Progress in Additive Manufacturing (2024) 9:857–874
https://doi.org/10.1007/s40964-023-00486-9

FULL RESEARCH ARTICLE

Biopolyamide composites for fused filament manufacturing: impact of fibre type on the microstructure and mechanical performance of printed parts

Karina C. Núñez Carrero[1,2] · Manuel Herrero[1] · Luis E. Alonso[1] · Félix Lizalde-Arroyo[1] · Leandra Oliveira Salmazo[1] · Juan Carlos Merino[2] · Miguel Ángel Rodríguez-Pérez[1] · José María Pastor Barajas[2]

Received: 14 March 2023 / Accepted: 29 June 2023 / Published online: 7 July 2023

Abstract

As additive manufacturing (AM) becomes more widespread in ever more demanding applications, the performance demands on printed parts are increasing. Efforts are directed towards improving mechanical performance in all manufacturing directions, including requirements such as sustainability, economic viability, and weight savings. This work focuses on the systematic study of printed parts by manufacturing fused filaments fabrication (FFF) of a bio-based polyamide (PA11) reinforced with different types and amounts of fibres: short glass fibre (GF) and a needle-shaped nanofibre: sepiolite (SEP). The aim was to establish which of these two had the best balance between improving mechanical properties and forming intra- or interrater defects. The surprising results revealed that the different morphologies of these fillers induce two opposite stiffening mechanisms and defect microstructure. In the case of SEP, a change in the crystalline polymorph, a higher crystallisation rate and the elevated dispersion of high and constant surface area fibres increase the stiffness at a lower effective load. Additionally, nanocomposites possess lower percentage porosity with more isotropic and smaller average inter-raster pores compared to GF composites. The latter are stiffened only by the immobilisation effect of the confined polymer chains in a system with a high dispersion of fibre sizes with heterogenous and intrarasterised defects. By contrast, these morphologies provide the GF composites with a more effective energy dissipation mechanism in impact tests and higher thermal stability.

✉ Karina C. Núñez Carrero
karinacarla.nunez@uva.es

[1] Department of Condensed Matter Physics, Cellmat Laboratory, University of Valladolid, 47011 Valladolid, Spain

[2] Foundation for Research and Development in Transport and Energy (CIDAUT), 47051 Valladolid, Spain

Graphical abstract

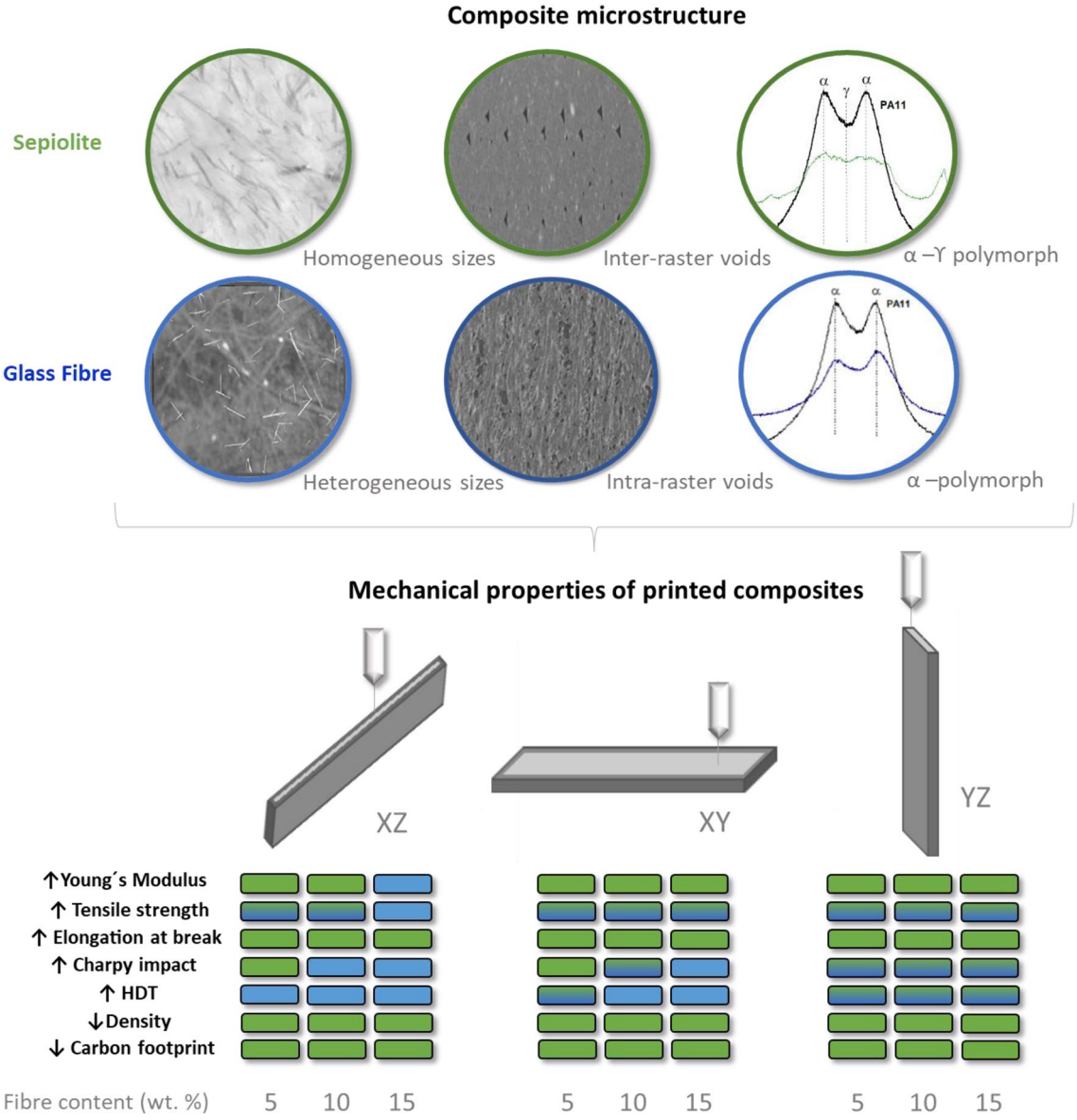

Keywords Fused filament fabrication (FFF) · Fibre-reinforced polymer · Nanocomposites · Biopolyamide · Mechanical properties · Thermal properties

1 Introduction

First introduced in the 1980s to meet the highly specialised needs of rapid prototyping and modelling, additive manufacturing (AM) or 3D printing has now become a versatile technology platform for the manufacture of complex parts. AM enables the production of custom parts without the need for tooling associated with conventional formative and subtractive manufacturing. In addition, it offers the possibility to build complex geometries at lower cost, with less scrap material, shorter lead time and fewer assembly requirements [1–4]. Among all the AM technologies, Fused Filament Fabrication (FFF) is the most mature technology [5–7]. FFF relies on the extrusion of a thermoplastic filament melt through a nozzle and the selective deposition on a surface to build up a part in a layer-by-layer manner [8, 9]. In the past, FFF was mainly used for prototyping [10, 11]. However, nowadays its use in the production of plastic parts [8, 12] is spreading, due to the opportunities for mass customization of the parts,

the decrease in energy consumption, and improved materials' utilization [2, 3]

The two most common polymers used in FFF are poly(acrylonitrile-co-butadiene-co-styrene) (ABS) and poly (lactic acid) (PLA) [9, 13]. However, they tend to be limited by their low-operating-temperature ceiling and insufficient mechanical strength for engineering applications [14]. For this reason, research into new materials for FFF continues, driven by several factors, primarily increased functionality [15], improved mechanical performance [16] and increased operating temperature range [17]. In recent years, polyamide-based materials have received special attention. The family of polyamides is characterized by their good mechanical performance, at a reasonable cost, and good thermal and chemical resistance. In AM, polyamide-12 is widely used for selective laser sintering (SLS) technology [18, 19]. However, there are not much available polyamide materials for printing by FFF. There are some examples of polyamide-6 and polyamide-12, but these materials are specially designed for professional production in high-cost 3D-printers [20]. The lack of polyamide materials for FFF is due to its water-absorbing trend and crystallization behaviour that led to important problems of deformation when it is deposited on the printing bed [21–23].

The selected polyamide for this work is the commercial bio-based PA11, which is synthesized using the 11-aminoundecanoic acid from castor oil. This provides a fully renewable and sustainable polymer with large-scale production [24]. Besides the natural origin, the larger length between amine groups, compared with most conventional polyamides (6 and 66) leads to lower water absorption and better chemical resistance. Additionally, PA11 is of great importance because of its excellent properties, including resistance to chemicals, a wide range of working temperatures and high dimensional stability. Hence, this type of polyamide is willingly used in almost every industrial sector, for instance, automotive, industrial vehicles, medicine, food packaging, aerospace, sports applications, and also textile industries.

In addition to addressing sustainability requirements with the study of bio-based polymers, general mechanical requirements are addressed with the strategy of creating composites based on a polymer matrix and different reinforcements [7, 25] to strengthen 3D-printed parts and provide added functionalities. These composites are desirable, because they provide a different approach to modulating the properties of the 3D-printed part from the composition. Although several discontinuous fillers, such as graphene, wood, carbon fibre, glass fibre, nanoparticles, etc. are commercially available and are widely studied in the manufacture of parts from matrices such as PLA and ABS by FFF, they generally increase the cost of the final material and their compositions are limited, as they modify the rheology necessary for filament deposition, increase the density and their large sizes affect the final porosity of the part and thus its final performance. Even so, their nucleation and stiffening capacity is widely reported among the commodity polymers used in FFF [26].

In this work, the effect of different fibre types on PA11 has been evaluated. Glass and needle-shaped nanoclay were selected as reinforcement fibres for PA11 composites. On one hand, E-glass was selected as the most conventional fibre for polyamide reinforcement. The use of polyamide/glass fibre composites is widely spread in different industrial sectors, mainly in applications where strength and high service temperature are demanded. On the other hand, sepiolite was selected as nanometric scale fibre. Sepiolite is a natural mineral clay, with needly like shape due to its internal structure [27]. Traditionally, layered nanoclays have been the most used for reinforcing polyamides [28]. However, it has been demonstrated that fibrous nanoclays lead to a better mechanical performance in the final polyamides nanocomposites [22, 29]. For both, glass fibre and sepiolite, even without surface treatments, it has been demonstrated excellent compatibility with the polyamide matrix. This phenomenon is due to the arrangements between the hydroxyl groups of sepiolite surface and the amide polymer groups.

Our research group reported for the first time the use of nanoclays in the manufacture of BIOPA11 composites for additive manufacturing by FFF [21]. The results demonstrate the potential of sustainable nanocomposites for additive manufacturing via FFF. This new study is focused on making a comparison between the effect of a nanometric and a millimetric fibrillar reinforcement in bio-based polyamide matrix (PA11) to obtain pieces by FFF. The specific areas of these fillers, together with the printing process, play a fundamental role in the thermal and mechanical behaviour of the final parts. There is numerous bibliography that separately establishes the effect of different type of reinforcement, in polymeric commodity matrices type, e.g., PLA, ABS, etc. [26, 30] But until now, none of them established a comparison, explaining from a microstructural point of view, the differences between composites and nanocomposites, using a bio-based matrix. This research arises from the urgent need to lighten weight, reduce costs, and increase sustainability in the production of plastic parts, including the substitution of synthetic fibres such as GF and the use of bio-based matrices.

To validate the use of these composites, test samples were printed in different orientations and subjected to a comprehensive characterisation programme based on tensile, Charpy impact and heat distortion temperature (HDT) tests. The results obtained have been related to the microstructural changes obtained, both in the polymer (rheological and thermal properties) and in the porosity of the final part (morphology of the inter- and intrarasters voids).

It was observed that each type of fibre acts differently on the PA11 and the morphology of the printed part. A complex relationship between type, amount of fibre and printing directions has been described whereby improvements in stiffness, impact properties and service temperature can be modulated by controlling the type and amount of fibre in the final biocomposite.

2 Materials and methods

2.1 Materials

The commercial fully bio-based polyamide used in the study as a polymer matrix was Rilsan PA11 BESNO from Arkema (MVR: 1cm^3/10 min, density: 1020 kg/cm^3). The nanofibre used for the preparation of the nanocomposites was a commercial Sepiolite (Pangel S9), without any surface modification (BET Specific surface area: 312 m^2/g, Average particle size—laser granulometry: 12.69 µm and Density in bulk: 2.0 g/cm^3) supplied by TOLSA S.A. (Spain). The type E glass fibre, 3 mm in length and with no surface modification (density 2.54 g/cm^3) was purchased from PPG.

2.2 Processing

2.2.1 Melt compounding

In order to prepare the composites, the as-received biopolyamide pellets and fibres were dried under vacuum at 80 °C for at least 16 h before processing. The dried materials were fed into a co-rotating twin-screw extruder, model Leistritz 27 GL (L/D = 36), operating at previously optimized conditions to ensure good dispersion of the sepiolite and the glass fibre within the polyamide matrix (the extrusion temperature profile ranged from 235 to 250 °C and all the materials were extruded at 150 rpm) [22]. Three different composites for each type of fibre were produced. The neat PA11 was manufactured using the same procedure to ensure the same thermal history.

The final fibre content of the nanocomposites was determined by thermogravimetric analysis (TGA, Mettler Toledo TGA851). All the samples were submitted to a controlled temperature program from 25 to 900 °C at a heating rate of 10 °C min^{-1}, in a nitrogen atmosphere. The TGA results of the prepared materials are shown in Table 1.

Table 1 The final content of fibres in the obtained composites

Sample	Type of fibre	Final fibre content (wt.%)
PA11	None	0.0
5 wt.% SEP	Sepiolite (SEP)	3.9 ± 0.2
10 wt.% SEP	Sepiolite (SEP)	8.8 ± 0.3
15 wt.% SEP	Sepiolite (SEP)	14.2 ± 0.2
5 wt.% GF	Glass fibre (GF)	6.0 ± 0.4
10 wt.% GF	Glass fibre (GF)	10.3 ± 0.3
15 wt.% GF	Glass fibre (GF)	15.2 ± 0.6

2.2.2 Preparation of filaments

The pellets of the composites obtained in the previous step were dried under vacuum at 80 °C for 16 h before filament preparation. The filaments of bio-based polyamide and its composites were produced using a FILABOT EX6 setup based on the following components: a single-screw extruder machine for melting, an airpath for cooling, a thickness gauge, and a spooler for winding. The extrusion temperature profile, for all the filaments, was from 185 to 200 °C, while the relationship between speed extrusion and spooling was optimized for obtaining filaments with 1.75 ± 0.03 mm thicknesses.

2.2.3 3D printing (FFF)

After a drying process, 16 h in a vacuum oven, all the filaments were printed using a homemade 3D printer designed and manufactured by CIDAUT Foundation (see Fig. 1a). The printer is specially designed to control the humidity and the temperature inside the printing chamber for avoiding thermal stress and warping. The filaments were fed from the spool to the nozzle by pinch rollers. The filament runs this path enclosed in Teflon pipes to prevent damage during printing. The selected processing conditions for all testing samples are shown in Table 2. As testing specimens, square prisms (100 × 15 × 3 mm^3), in the three possible directions (Fig. 1b) were printed for tensile, heat distortion temperature (HDT) and Charpy impact test. All printing conditions were chosen based on previous results [21]. In this case, the dimensional stability of the parts has been improved with the use of a chamber (100 °C) and screen angles of – 45°/+ 45° to improve the mechanical response.

2.3 Characterization

2.3.1 Tensile tests

The tensile test program was used to study the influence of fibre type, amount of fibre and printing orientation in the final mechanical properties of the printed parts. ASTM D3039 procedures were followed for testing. All the tests were carried out at 25 ± 2 °C and relative humidity of 50 ± 5% with an Instron Model 5567 (1 kN load cell) at

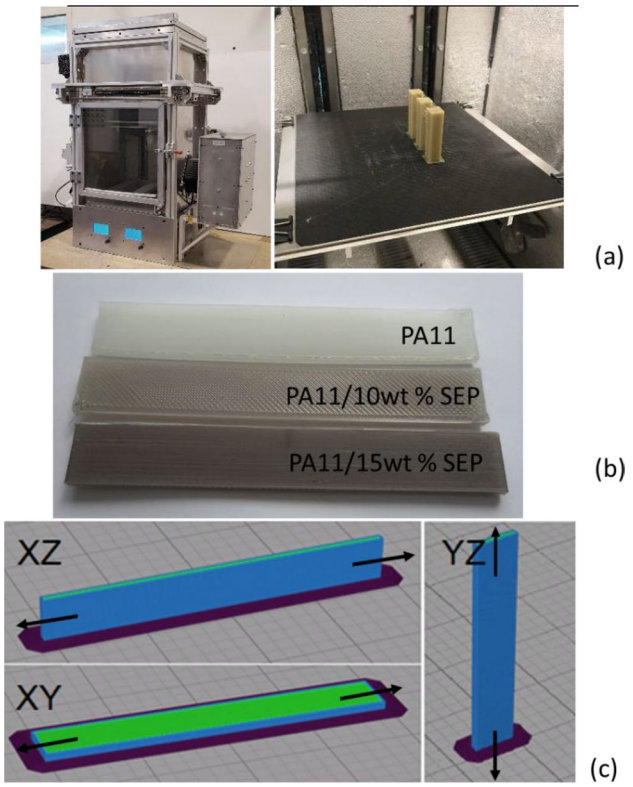

Fig. 1 **a** Used homemade 3D-printer, view outside and inside the chamber **b** dimensionally stable printed end-pieces and **c** Different orientations of the tensile bars printed for mechanical testing, where the contour is presented in blue colour (0°) and infill in green colour (− 45°/+45°). The arrows show the direction of the tensile stress used in the characterisation

Table 2 Processing conditions of the printed test specimens

Printing parameter	Choice
Build style	Solid normal
Infill density (%)	100
Extrusion temperature (°C)	240
Chamber temperature (°C)	100
Layer thickness (mm)	0.30
Raster width (mm)	0.60
Raster angle (°)	− 45°/+45°
Contour (mm)	0.60
Printing speed (mm/s)	30

10 mm min^{-1} following ASTM D638 procedures. For each composition and print condition, at least ten specimens were tested, and mean values of the properties were reported. As a function of the direction and amount of loading, the improvement efficiency index (IEI) of the tensile properties was measured as described in Eq. 1.

$$\mathrm{IEI} = \frac{\text{Achieved property}}{\text{Initial property}}. \quad (1)$$

2.3.2 Heat distortion temperature (HDT)

The service temperature of the composites was measured in a CEAST HDT3-VICAT P/N 6911/000, using a 1.8 Mpa load, according to ISO 75. Three specimens were tested for each composite and printing orientation, and mean values were calculated.

2.3.3 Impact properties

The notched Charpy test values were measured in a Resil 6957 impact pendulum at room temperature according to ISO 179. At least ten specimens were tested for each nanocomposite, and mean values were reported along with the standard deviation in values.

2.3.4 Microstructural characterisation

The effect of the sepiolite and glass fibre content on the crystallization of the PA11 was measured by differential scanning calorimetry (DSC, Mettler Toledo DSC 851e) from 25 to 250 °C at a heating rate of 20 °C min^{-1} under nitrogen flow. Only the first endotherm was evaluated to determine crystallisation in the final printed part. The selected enthalpy of fusion for perfect PA11 crystal was 189 Jg^{-1} [31]. The dispersion of the sepiolite in the nanocomposite was confirmed by transmission electron microscopy (TEM, JEOL JEM-1011HRP) operating at 100 kV.

In order to study the energy dissipation during the impacts, the surfaces of the tested specimens were analysed by Scanning Electron Microscopy (SEM). In the first step, the surfaces were treated using a sputter coater POLARON SC7640. Then, the impact surfaces of the samples were studied by using a scanning electron microscope (Hitachi S-3400N).

The WAXS measurements were carried out with a Siemens D500 apparatus. For the measurements, a CuKα radiation (40 kV, 15 mA), and the scanning rate was 4°/min.

The internal structure of the printed parts was obtained by tomographic characterisation, using the procedure described by Pérez-Tamarit et al. [32]. The equipment consists of a micro-focus cone-beam X-ray source L10101 from Hamamatsu (spot size: 5 µm, voltage: 20–100 kV, current: 0–200 µA) with a maximum output power of 20W and a flat panel detector C7940DK-02 also from Hamamatsu (2240 × 2344 $pixels^2$, 50 µm of pixel size). The X-ray projections were acquired in 0.3° increments over 360° of rotation and the source operated at 50 kV/170 mA. After the experiment, the shape was reconstructed using

the "Octopus Reconstruction" software to obtain the YZ and XZ map of samples. The analysis of the reconstructions was carried out by evaluating several images using ImageJ and Fiji software. The anisotropy coefficient between any two directions (e.g., *X* and *Y*: AR (*X*)/(*Y*)) was defined as the cell size in the X direction divided by the cell size in the Y direction.

To measure the fibre size of the final GF composites, the samples were calcined in a Hobersal model HD230PAD vacuum furnace at 800 °C and the resulting fibres were evaluated under a ZEISS STEMI 2000 optical microscope with OMNIMET image analysis software.

Finally, a shear stress-controlled rheometer (AR 2000 EX from TA Instruments) was used to measure the viscosity of the composites in a strain sweep test at 240 °C and 1 rad/s.

3 Results and discussion

3.1 Relationship of composite microstructure to tensile properties

Figure 2 shows the tensile properties of the printed composites in the three possible orientations. As widely reported, increasing the amount of fibres (regardless of their nature:

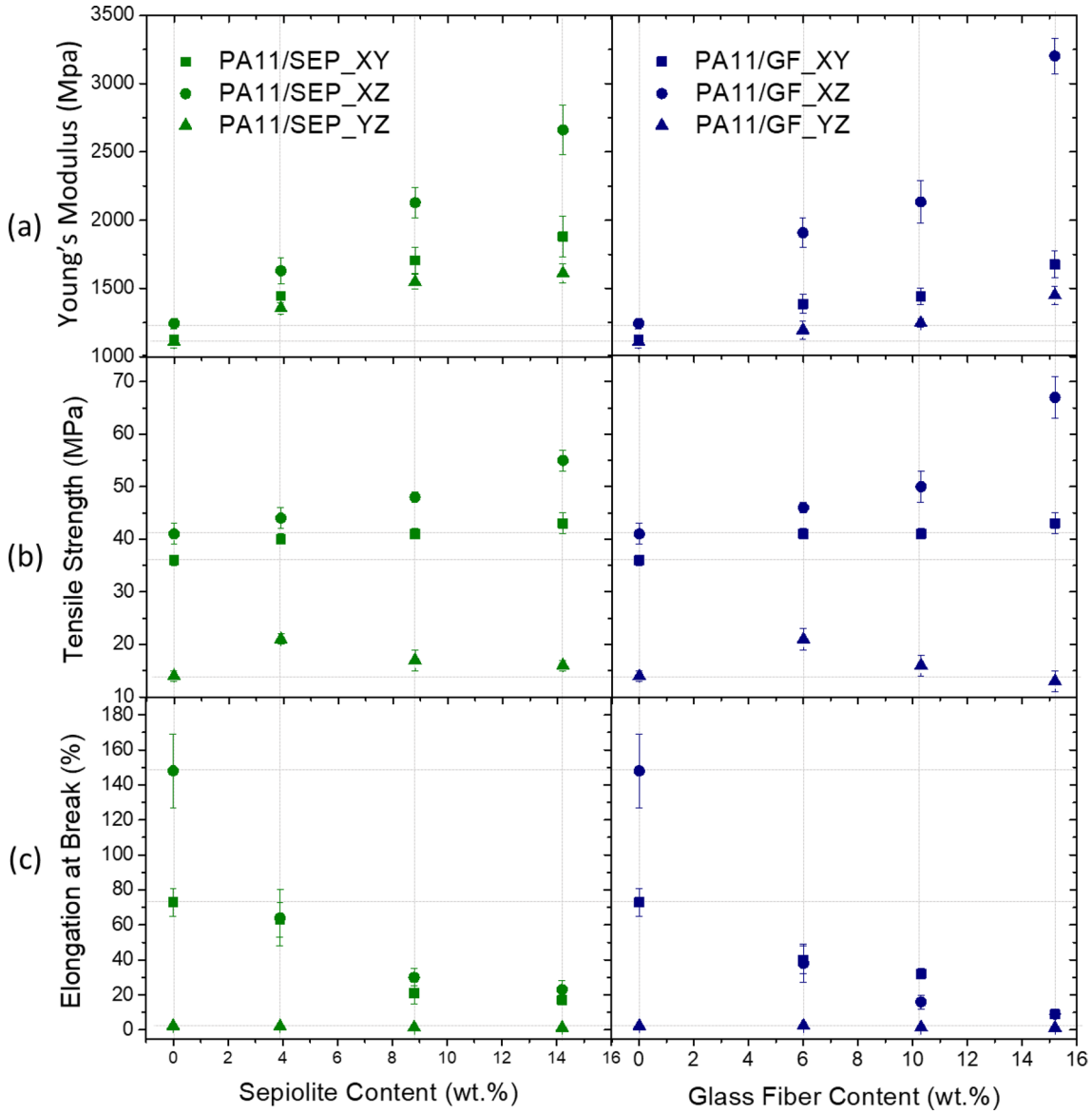

Fig. 2 Tensile properties of the sepiolite nanocomposites (left) and glass fibre composites (right) as a function of the reinforcement content: **a** Young's modulus, **b** tensile strength and **c** elongation at break

sepiolite or glass fibre) in the polymer composites leads to higher Young's modulus stiffness and tensile strength values (see Fig. 2a, b). On the other hand, fibres also lead to a significant decrease in the elongation at break values of specimens during tests (see Fig. 2c).

As can be seen in Fig. 2a, the modulus values increased following a linear trend with the amount of fibre. Two phenomena are responsible for this fact: the effect of load nucleation and the immobilisation of the polymer chains by the solid particles [33]. For sepiolite-reinforced samples, the addition of 14.2 wt.% of nanofibres led increments from more than two-fold (in *XZ* direction) to 45% (in *YZ* direction), while 15.2 wt.% of glass fibre led increases from more than two-fold (in *XZ* direction) to 30% (in *YZ* direction) in comparison with the neat bio-based PA11. The modulus values analysis shows that SEP nanocomposites present better results than GF composites for similar loading amounts. Besides, this trend was observed for all the printing orientations. However, there is a discordant point for the composite reinforced with 15 wt.% of glass fibre printed in *XZ* orientation.

It cannot be concluded that in the printed composites, the increase in Young's moduli responds to the increase in crystallinity. Neither sepiolite fibres nor glass fibres are able to nucleate the structure, as the thermal DSC tests showed little significant changes in enthalpy and peak melting temperatures (see Fig. 3a). However, in the case of nanocomposites, it is important to note the small shoulders appearing in the melt endotherms, in addition to the directly proportional increase of the crystallisation rate with the number of nanoparticles, which act as heterogeneous nucleation sites [34] (see green lines in Fig. 3b). These phenomena are not as noticeable in glass fibre-reinforced composites. It is important to mention that the thermal analysis was performed on the filament. In the supporting information S1, the quantitative data of this analysis is tabulated. Additionally, the thermal analysis on the printed parts, in the different directions has been included. No significant changes with printing direction are reported.

In order to associate the DSC curves observations with the increased stiffness of the printed nanocomposites, the crystalline system was studied. Figure 4 shows the results of the WAXS analysis performed on the PA11 composites. The main crystalline peaks in the spectra were observed at $2\theta = 20.5°$ and 23.5° corresponding to the (100) and (010/110) planes, respectively. These crystalline peaks correspond to the α-polymorph of PA11 [35]. The addition of GF maintains the stable α-triclinic configuration of PA11, but its presence perturbs the crystallisation, considerably decreasing the area under the curves, which implies that the size or perfection of the crystals is smaller than that of pure PA11, but without inducing a change in polymorphism. Therefore, GFs improve stiffness only because they restrict the movement of the chains, and this is greater the higher the amount of loading.

However, although the sepiolite nanocomposites maintain the trend of decreasing crystallinity, because it acts as a defect of the crystalline system as well as GF composites; a broadening of the peaks is observed in the nanocomposites (see Fig. 4b), which predicts a more heterogeneous crystalline system and the crystalline transition from α to γ (or α`[33]) form, independent of the printing orientation (see zoom in Fig. 4c). These broad signals are absent in the WAXS patterns of PA11 or GF composites, which have been processed in the same way.

The γ crystalline phase is metastable and consists of random hydrogen bonding between parallel chains in the Polyamides [36]. Both crystalline phases (γ and α) have been reported to exhibit different mechanical properties. The α phase exhibits a higher modulus below T_g but a more rapid

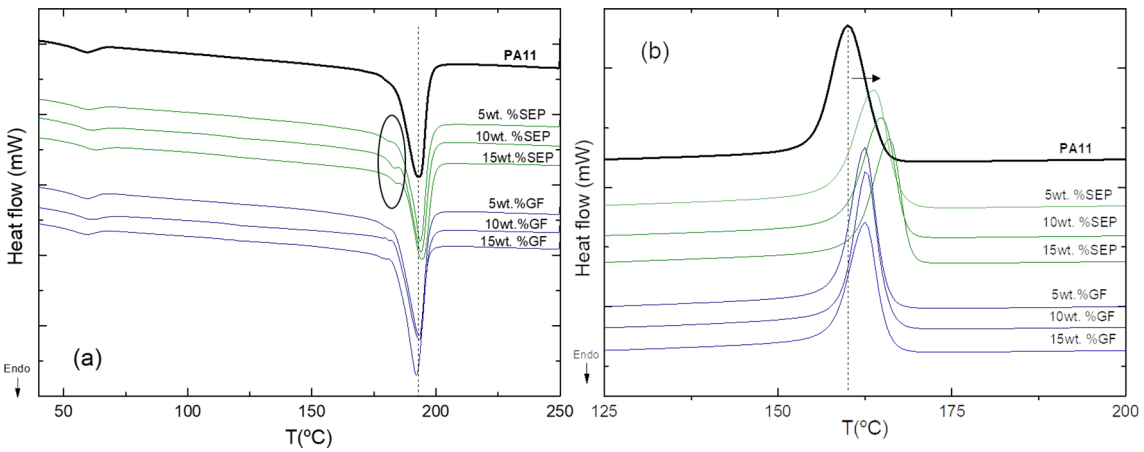

Fig. 3 DSC thermograms of the SEP nanocomposite filament and the GF composite filament for **a** the melting endotherms and **b** the crystallisation exotherm

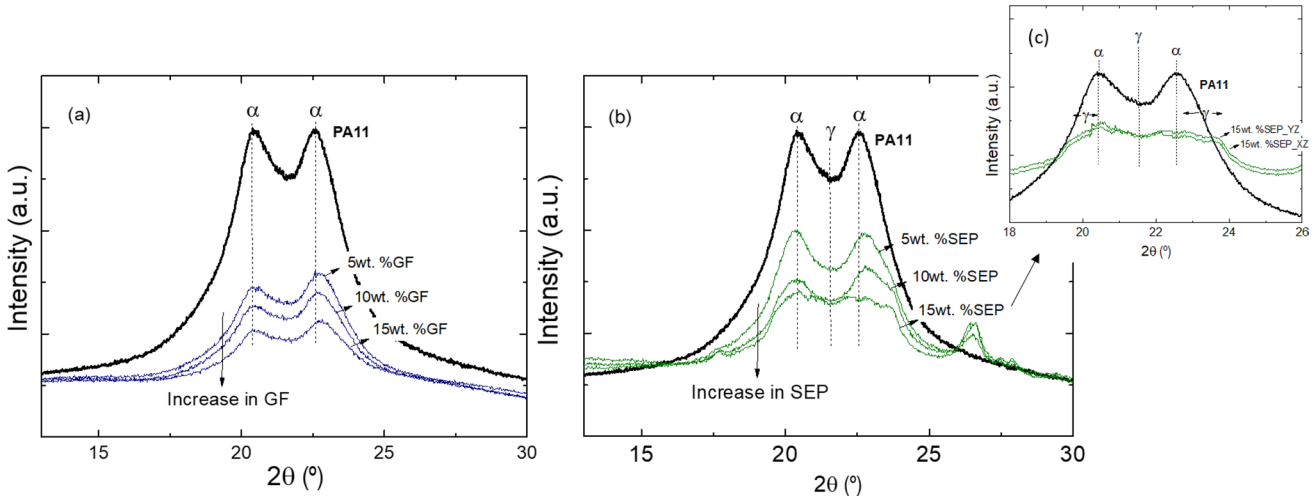

Fig. 4 WAXS pattern of **a** GF composites, **b** SEP nanocomposite and **c** comparison of the peak morphology of the 15wt.% SEP nanocomposite in two different printing directions compared to the peaks of PA11pure

decrease above T_g than the γ phase. This implies that the γ phase has a higher heat distortion temperature [37]. However, with the amount of sepiolite and under the crystallisation conditions studied, this phase is unstable, and its effect is not as marked as reported for other PA11 nanocomposites with other types and amounts of fillers [38, 39] or isothermally crystallised [38, 40, 41]. The differences in the types of polymorphs obtained agree with other reports which have indicated that the crystalline structure of PA11 is generally affected by processing conditions (annealing, high pressure, etc.) [42].

These changes in the crystalline polymorph may be responsible for the competitiveness of SEP as a reinforcement for PA11 printed parts versus GF (which is denser, more expensive and has a higher carbon footprint in use). Furthermore, these stiffening phenomena occurring without increased crystallisation are desirable in additive manufacturing to avoid shrinkage in the deposited filaments.

On the other hand, it is important to mention the difference between the sizes, surface areas and compatibility of the fibres studied in the printed PA11 composites. The favourable enthalpy associated with hydrogen bonding between the amides in the matrix and the surface hydroxyls of the fibres promotes high compatibility and dispersion in the matrix (i.e., GF composite, Fig. 5a, b) [29]. However, the higher surface area of SEP compared to GF enhances these interactions and the immobilisation of the polymer chains, making it very competitive at low concentrations. In the TEM micrographs of Fig. 5c, the high dispersion achieved in PA11/10wt.% SEP, responsible for the crystalline defects and polymorphism previously described, can be observed. However, as mentioned above, the compounds with 15wt.%

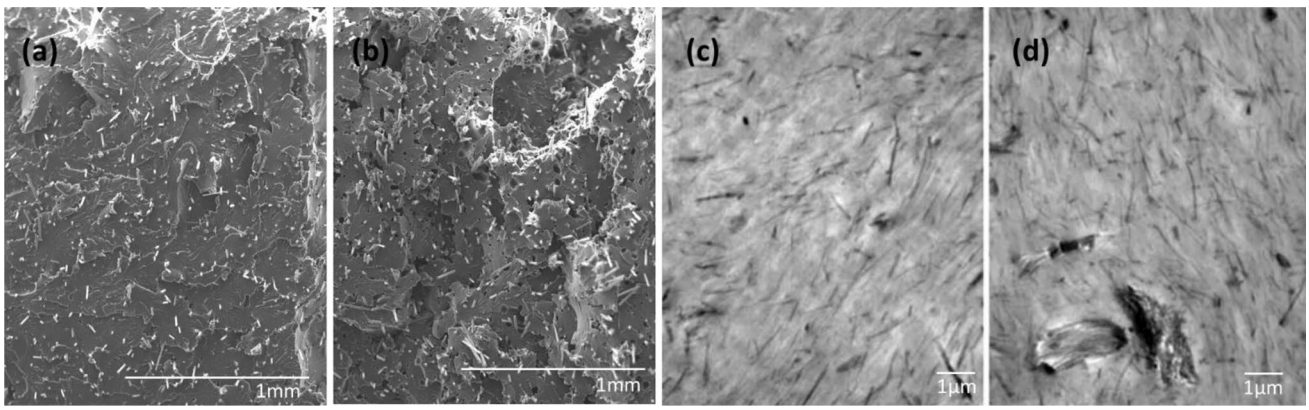

Fig. 5 Dispersion and distribution of fibres in the polymeric matrix of the composites. SEM images for composites with **a** 10wt. % and **b** 15wt. % of GF. TEM images for nanocomposites with **a** 10wt. % and **b** 15wt. % of sepiolite

GF presented a higher modulus than the SEP analogues (see Fig. 2a). This phenomenon may be due to the higher alignment of the glass fibres during printing because of their longer length and higher content (see Fig. 5b) [43]. Finally, there is an increased likelihood of sepiolite aggregates forming when high amounts are used in the nanocomposite [44] (see Fig. 5d). This point of view, together with the aspects discussed above, makes it possible that at higher loading concentrations, GF nanocomposites are stiffer.

On the other hand, it is important to consider GF breakage with processing (different shearing and heating cycles have been used for the production of composite materials: composites obtaining, filament making and printing parts). Due to the increased interactions between the fibres, the surfaces of the mixing equipment and the polymer matrix with a high filler load, the size of the fibre is significantly reduced. Damaged and smaller reinforcement fillers provide lower reinforcement effects to the printed composite parts, leading to lower mechanical performance [30]. Figure 6 shows this phenomenon in the studied GF composites, the average length of the pristine GF (blue bars) is close to 3.0 mm, while in the final 15wt.% GF composite, the average fibre length is close to 1.0 mm (grey bars). This means that composite materials are being compared, not only with different amounts of GF but also with different sizes. This makes the comparison complex. Finally, it is shown that the FFF technique does not exploit the advantages of GF length when large quantities are used.

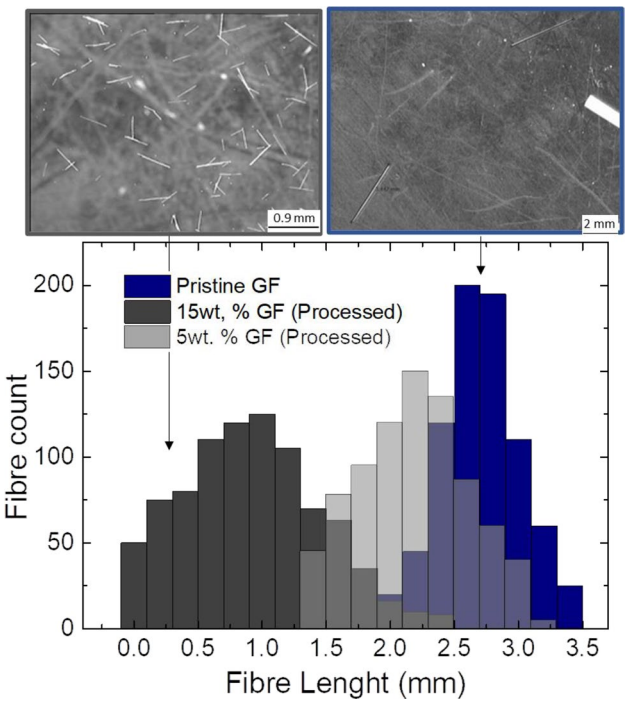

Fig. 6 GF size distribution for pristine GF (blue bars), 5 wt.% GF composites (light grey bars) and 15 wt.% GF composites (dark grey bars)

Having discussed the effect on tensile properties of the type and amount of load, it is important to describe the relationship of the loads to the different print orientations. In this sense, better results were obtained for samples printed in the *XZ* direction (see the symbol ●, in Fig. 2), while the worst results were shown by samples printed in *YZ* (see the symbol ▲, in Fig. 2). This phenomenon is due to in *XZ*, almost of the filaments, that constitute the tensile bars, have been deposited in the direction of the applied force during testing. On the contrary, for samples printed in *YZ*, all the filaments were deposited perpendicular to the applied strain and the fibres are not as effective at carrying the load in this orientation. At this point, it is important to note that reached modulus values of the neat PA11, printed in *XZ*, were similar to the values shown when the samples are obtained by injection moulding [21] (see Supporting Information S2), which corroborate the selection of adequate printing conditions.

Many authors have reported that Young's modulus and tensile strength of printed samples in the *XY* and *XZ* orientations depend mainly on the strength of the starting materials, while the strength in the *YZ* orientation is mainly determined by the inter-rasters bond strength controlled by the fusion bonds between adjacent frames [25]. Therefore, the strength in the *Z* orientation is lower than in the other orientations, as the inter-rasters bond strength is always lower than the strength of the base material [45, 46] An improvement of the mechanical properties in the *YZ* orientation of FFF-printed parts has been reported due to the use of reinforcements at the interfaces between filaments [47] as it promotes better molecular diffusion of the polymer and cross-linking across the interface due to a better thermal conductivity of the printed composite parts at low filler concentration [48] It can be seen from the data representing the stiffness at *YZ* (see the symbol ▲) in the graphs of Fig. 2a, sepiolite is the best performing reinforcement in this critical orientation. It should not be forgotten that the design of a part is made according to its lower properties, therefore, more attention needs to be paid to the improvement of the *Z*-strength of the parts printed with FFF.

To obtain an overall view comparing the effectiveness of both reinforcements studied on the stiffness of the printed parts in different printing orientation and fibre amount, the Improvement efficient index (IEI) has been calculated (see Fig. 7). The graphs show the rate of variation of the properties concerning the original polymer matrix. The graphs show that in the most critical direction *YZ*, the SEP also offers the greatest increase in Young's Modulus, regardless of the amount of fibre (Fig. 6a), as well as having the highest values as described above. An important detail is that the nanocomposites always have a lower effective loading in the final composite than the GF analogues (more complex

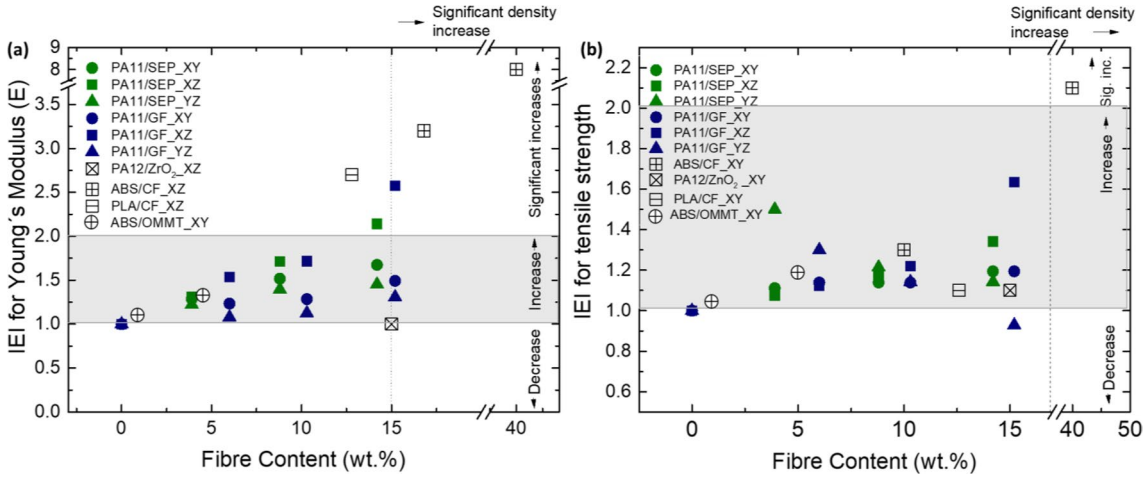

Fig. 7 The plot of **a** IEI value of Young's Modulus and **b** EIE value of tensile strength versus fibre content

dosage during compounding); this also influences the properties obtained and makes the nanoparticles even more competitive.

The shaded region in Fig. 7a, b indicates the area where most of the reported polymer composites with different discontinues fibres by FFF, which are considered successful ($1 < IEI < 2$) [26], are concentrated. The biocomposites discussed in this study are perfectly contained in this area. When the IEI obtained are compared with some data reported outside that zone, it is observed that it is necessary to use large amounts of fibre, compromising the density, processability, sustainability and cost of the printed parts (e.g., ABS/CF; 20 or 40wt.% carbon fibre). On the other hand, PA11 nanocomposites appear to be quite competitive compared to PA12 and PLA composites in the *XZ* direction and even to other nanocomposites such as nanoclay-reinforced ABS (ABS/OMMT) in the *XZ* direction [49].

Moreover, even though the addition of SEP and GF in PA11 maintains the anisotropic properties of the printed parts (see Fig. 2), the rate of enhancement in the nanocomposite appears to be more uniform in all directions than in the case of the GF composites (see how the green dots in Fig. 7a, b are closer together). Possibly, the morphological changes described above are responsible for this phenomenon (crystalline polymorphism, constant fibre sizes, etc.). But it is also important to consider that the mechanical strength of the FFF-printed composite is also determined by the final porosity of the material [50]. In order to evaluate the formation of voids due to the loads studied, an in-depth study of the defect microstructure of both composites was carried out in all directions and with different fibre contents.

The microtomographies in Fig. 8, show the typology and distribution of the voids formed inside of the different composites studied, in two different planes *YZ* and *XZ*, for the central sample area (zones closer to the edges of the samples were also analysed, see Supplementary Information S3). It is worth mentioning an important observation: regardless of the amount of fibre and the area where the micrograph was taken, there is a clear difference between the morphology of the defects in the SEP nanocomposites and the GF composites. In the former, more homogeneous inter-raster drop-shaped voids are observed, while in the latter, a heterogeneous structure with no defined inter- or intra-raster drop shape is observed. This can be attributed to the discontinuity of GF fillers (fibre length and amount) and lower chemical compatibility compared to SEP nanocomposites (due to their smaller surface area), which leads to a significant increase in intra-raster porosity [25, 30, 51]. Furthermore, this is explained by the fact that the higher number of GF generates more intra-raster voids at the edges or around the reinforcement, as the fibre and the polymer matrix can partially flow independently during the printing process [30].

Some authors recommend using a surface treatment on the fibres or choosing appropriate fibre sizes to improve fibre-matrix compatibility, which is as much a determinant in the mechanical properties of FFF-printed parts as interlayer compatibility [30]. In general, the volume fraction of voids in composite FFF-printed parts results from competitive shifts between large inter-raster voids and smaller intra-raster voids with increasing filler concentration [30]. In the GF composite, defect typology is marked by these phenomena. This does not occur in SEP nanocomposites.

It is also important to note that in GF composites, those with the least amount of filler are those with the largest and most elongated void sizes, which is consistent with the results obtained in Fig. 6: composites with the least amount of filler maintain the initial length of GF and these are deposited at the interface, creating a physical impediment in the layer-layer fusion, which replicates their elongated shape and larger size [26].

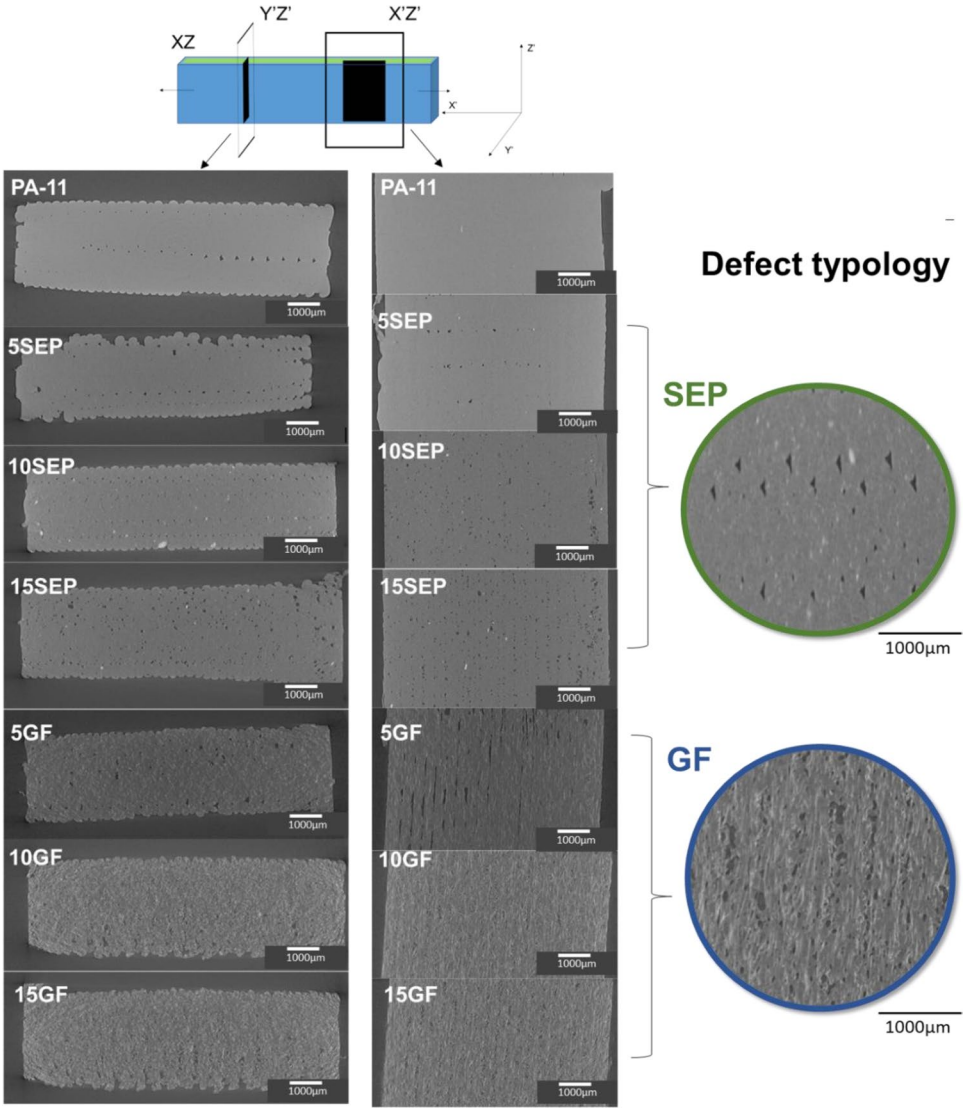

Fig. 8 Micro-CT images of printed PA11 composite specimens. The images were taken along the studied axes, inside the specimen. The representative image of the central zone is showed

In order to quantify the information obtained in the microtomographies, the images were analysed as described in the experimental section and the graphs in Fig. 9 were obtained from them. These graphs compare (a) the anisotropy of the voids, (b) the total percentage of porosity, (c) the average diameter of the pores and (d) the number of pores as a function of the type and amount of fibre.

From Fig. 9a, it can be clearly seen that, regardless of the orientation and amount of reinforcement, there are two different behaviours between SEP and GF composites. GF composites have more anisotropic defects than the voids of SEP nanocomposites. The irregularity and wide fibre size distribution in the final GF composite (see Fig. 6) may be responsible for its high defect anisotropy, as well as for the fact that there is no clear trend between void anisotropy and loading amount (see blue symbols in Fig. 9a).

In contrast, in SEP nanocomposites, as expected, defects are more isotropic in the orientation where they have the best mechanical properties (See the green symbols ● *XZ*) and less so in the direction where they have the worst (See the green symbols ▲*YZ*). Furthermore, the anisotropy is directly proportional to the amount of nanofibre, in all directions, due to the trend to agglomerate of the sepiolite (see Fig. 5). Still, the values for 15wt.% SEP are very close to pure PA11. This morphology can explain the performance of SEP as a system stiffener, as it offers the best ratio between the competing effects of stiffening and void formation.

Focused on porosity, independently of the type of reinforcement fibre, higher amounts lead a porosity increase; and this phenomenon is more pronounced in the case of GF (see Fig. 9b). It is widely reported that the increase of discontinuous fillers produces more pores inside the printed parts, due to the inhomogeneous dispersion of the fillers in the polymer matrix and the enlargement of pores around the fibres [25, 51] In the case of GF, the significant increase

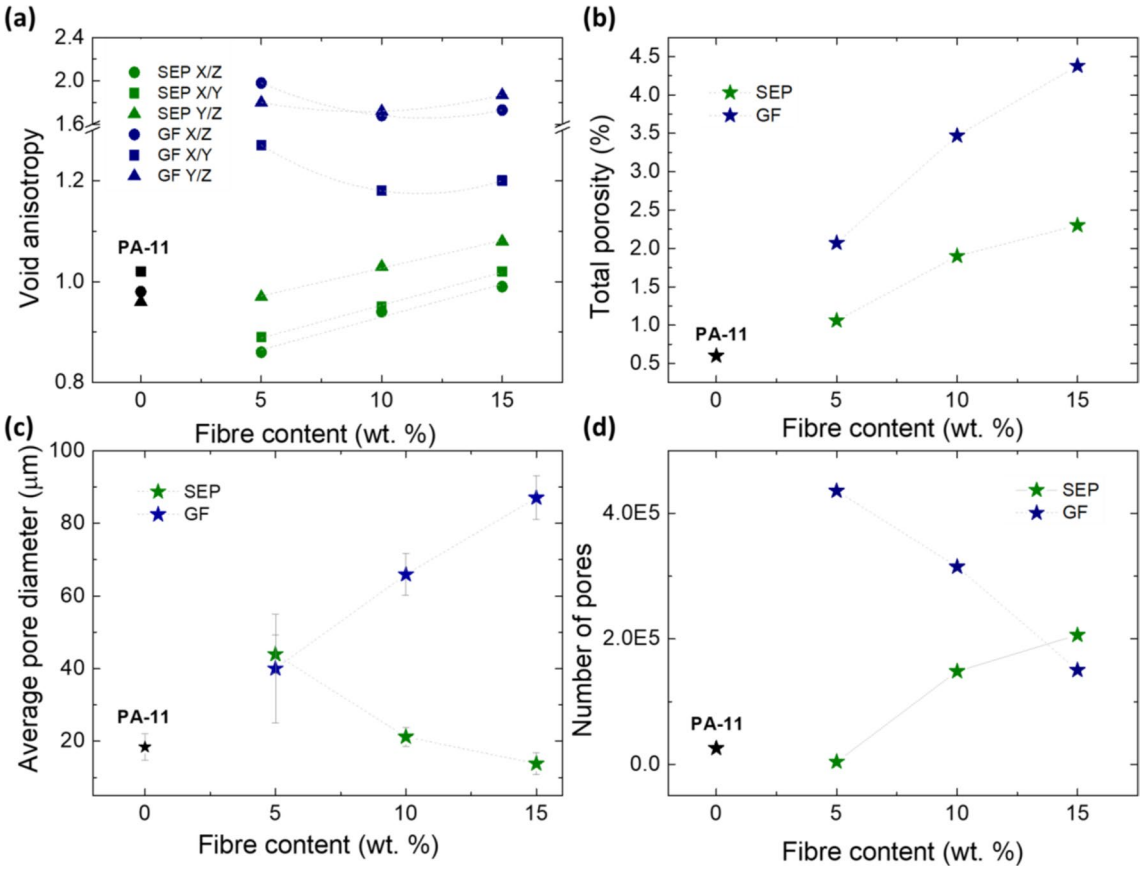

Fig. 9 Quantification of defect morphology **a** void anisotropy, **b** total porosity, **c** average pore diameter and **d** number of pores as a function of the amount of fibre

in intrarasterised porosity, shown in Fig. 8, is responsible for the higher % porosity than their sepiolite-reinforced analogues.

On the other hand, although in both composites, the porosity is directly proportional to the amount of fibre, in the SEP nanocomposite the number of pores increases while the average pore size decreases, while the GF composite decreases the number of pores, making them larger and larger as the amount of fibre increases (Fig. 9b, c and d). Thus, it is proved that two different behaviours occur within these types of composites. The correct dispersion of the sepiolite plays a fundamental role in the decrease of the pore size, the fillers can be homogeneously dispersed in the polymer matrix and the formation of voids caused by the introduction of the filler is kept low.

In order to explain the porosity of composites and its relationship with the stiffness obtained, it is important to consider that the introduction of fillers into the polymer matrix can increase the viscosity of the melt, leading to a reduced diffusion of the polymer between filaments. Similarly, segregated fillers at the interface with high loading can hinder inter-filament diffusion and act as stress points that generally weaken the interface and reduce polymer chain entanglements [25]. In this respect, rheological tests showed that, due to the low amounts of fillers used (less than 15wt.%), hardly any changes in the dynamic viscosity, measured at the printing temperature, were noticeable. Even for the composites with the highest amount of fillers (see Supporting Information S4). Therefore, the increase in viscosity did not play an important role in the formation of voids in the printed parts studied.

Finally, beside Young's Modulus and tensile strength, the elongation at break of these composites has been evaluated. The same behaviour is obtained as in composites obtained by other manufacturing processes: as the stiffness increases, the elongation capacity decreases. The decrease of the elongation at break with the rise of fibre content is shown in Fig. 2c. This trend has been widely reported [22, 43, 52]. The presence of reinforcement fibre produces a reversal from ductile to brittle, resulting in a drop in the elongation ability. This behaviour is clearly visible in the samples printed in *XY* and *XZ* orientations. In *YZ*, the samples failure at low deformation values ($\lesssim$ 3 wt.%) and consequently the trend is not observable. When comparing the values obtained for

the SEP and GF-reinforced specimens, higher values were obtained for the SEP nanocomposites. The morphology of the defects obtained, and the stiffening mechanism of the SEP nanocomposites compared to the GF composites explained above are consistent with this behaviour. When comparing macroscopically the tested specimens, it can be concluded that regardless of the type of fibre studied, in FFF the *XZ* direction always present more deformation capacity and this tensile property will be detrimental to the amount of load [26] (see Fig. 10).

3.2 Relationship of composite microstructure to impact properties.

Impact strength is employed to measure the ability of a specimen for absorbing energy and is an important factor for material selection in some specific applications. In this work, the printed samples were submitted to notch Charpy impact tests and the results are showed in Fig. 11. In the case of SEP nanocomposites (Fig. 11a), a clear negative trend of values was observed with increasing nanofibre content, especially for the samples printed in *XY* and *XZ* orientations. This trend follows the same behaviour observed for the injected nanocomposites based on polyamide matrices [53]. The embrittled with increasing amounts of sepiolite has been explained in terms of matrix-driven deformations [27], but

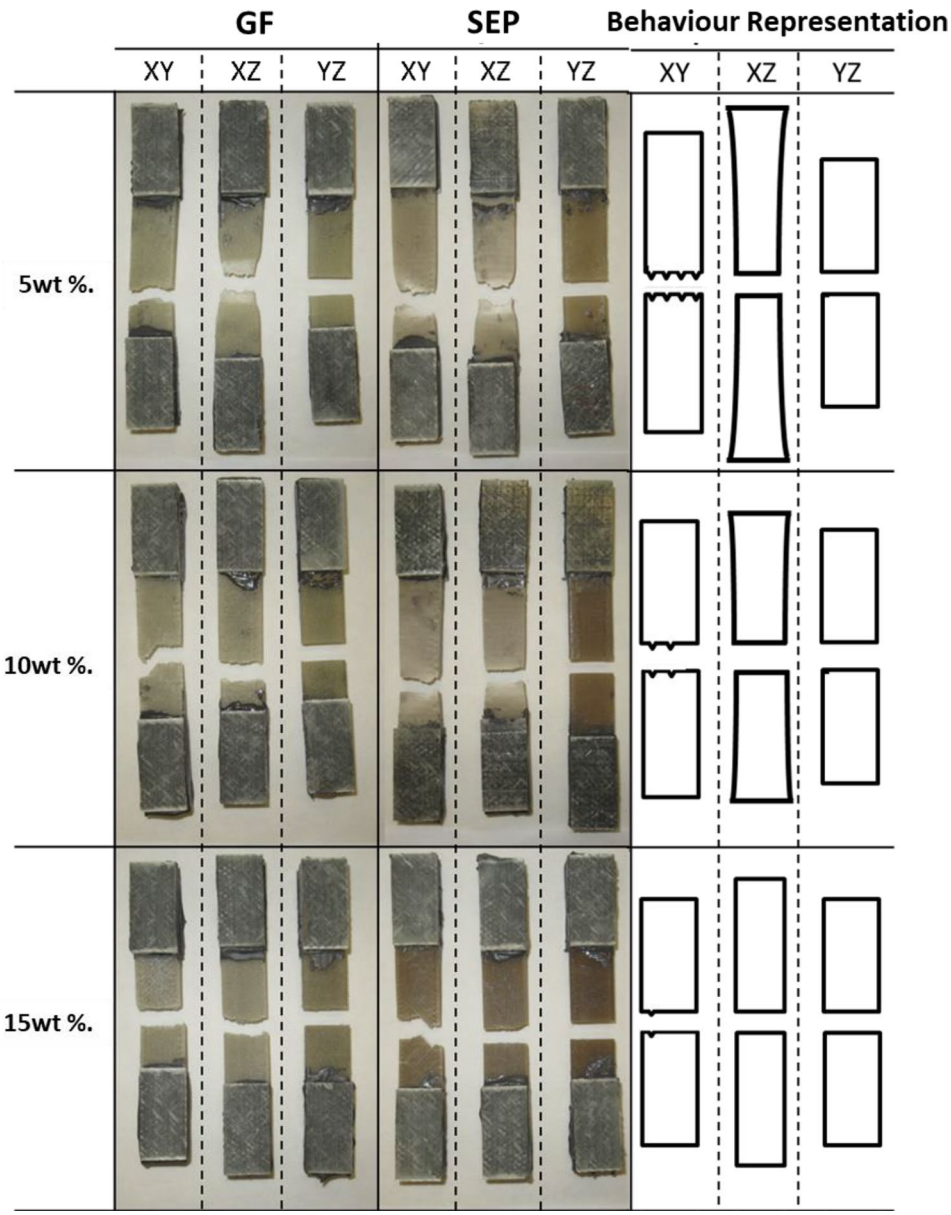

Fig. 10 Graphical representation of the tensile behaviour of all studied composites

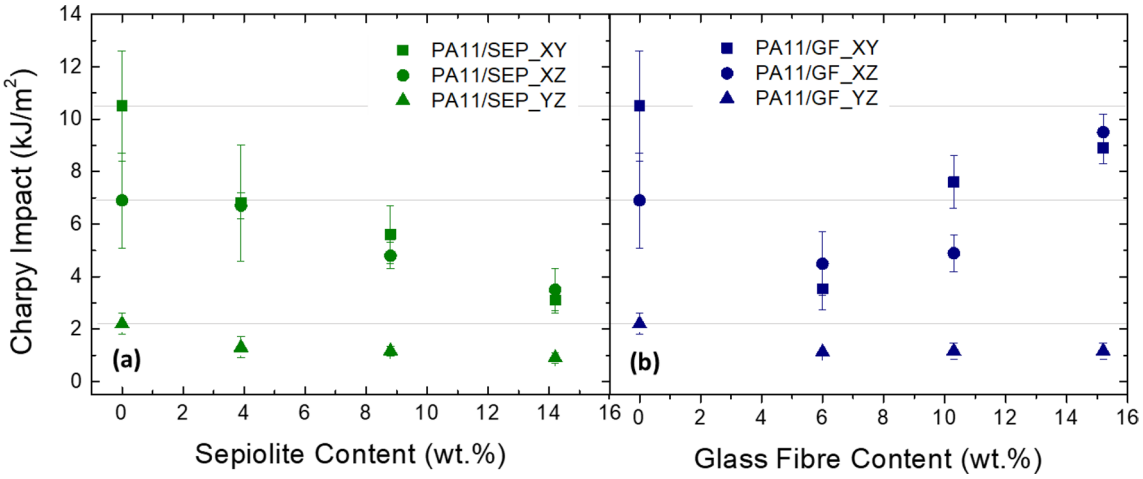

Fig. 11 Charpy impact values of the **a** sepiolite nanocomposites and **b** glass fibre composites as a function of the reinforcement content

also by the formation of micro-voids around the nanoclay, which coalescence together and give raises the formation of the crack [54]. According to these studies, the presence of nanofibres greatly reduces the deformation of the polymer matrix driving less ability to absorb energy during testing.

In the case of GF-reinforced composites, a completely different behaviour was observed. For a small concentration of reinforcement, a sharp fall in impact values was obtained. However, from about 6 wt.% of fibre, the impact resistance of the materials steadily rises until reaching similar values than neat polyamide for composites reinforced with 15.2 wt.%. This phenomenon has been reported before [55], and it is due to the fibres acting as crack initiators, but also hindering the propagation. At low concentrations of fibre, they act as structural flaws initiating the crack. However, the crack often must travel around fibres and higher concentration increases the path until reaches failure, which leads better energy dissipation [55–57] and consequently higher impact values. It is important to remark that once again the samples printed in *YZ*, irrespective of the type of fibre, showed the worst values and not a clear trend due to the failure occurring in the welding interface of two layers successively deposited.

To better understand the impact test result, the fracture surfaces of printed samples in *XZ*, where almost filaments were deposited perpendicular to test impact direction, were analysed by SEM (Fig. 12). As expected, the SEM image for the neat PA11 specimen (Fig. 12a) showed a smooth surface, which is consistent with homogeneous material. When sepiolite is added and the stress is applied, the coalescence of micro-voids leads to a rougher fracture surface (Fig. 12b). On the other hand, in the case of GF-reinforced composite, it can be observed that fibres are oriented (Fig. 12c, d). In this case, the multi-cavitation promotes plastic deformation in the matrix, hinders crack growth and generates a rougher surface. The multi-crazing phenomenon can disperse large amounts of impact energy, making PA six matrix easy to be deformed plastically [58]. This may explain the higher energy absorption when large amounts of GF are used.

As expected, increasing the load decreases this deformation capacity under load, even more so in the case of fibres with a smaller surface area such as GF. Furthermore, as has been shown, GF composites are more porous and have less compatibility at the fibre-matrix interface (see voids in the SEM image in Fig. 12d), which explains why GF composites are less ductile; on the other hand, their energy dissipation mechanisms mean that GF composites absorb more energy in impact tests with a greater amount of fibre.

3.3 Relationship of composite microstructure to service temperature

HDT is defined as the temperature at which the deflection of a standard specimen reaches 0.25 mm under a maximum applied stress of 1.82 MPa. Figure 13 shows the increase of HDT values with increasing nanofibre content in the biopolyamide matrix. It is important to note that, regardless of the printing orientation, all pure PA11 samples show the same value (≈ 45 °C). However, when the amount of SEP in the nanocomposite increases, the differences between the different printing orientations are much larger. These trends are caused by the aforementioned manufacturing orientation of the samples, but also due to the preferential alignment of the fibres in the printing orientation.

Once again, the best values were obtained for the specimens printed in *XZ* and the worst values were shown by the samples printed in *YZ*. When test specimens are printed in *XZ* orientation, the addition of 14.2 wt.% of sepiolite led to an increment of 83 wt.% in comparison with neat biopolyamide, while the sample reinforced with 15.0 wt.% of glass

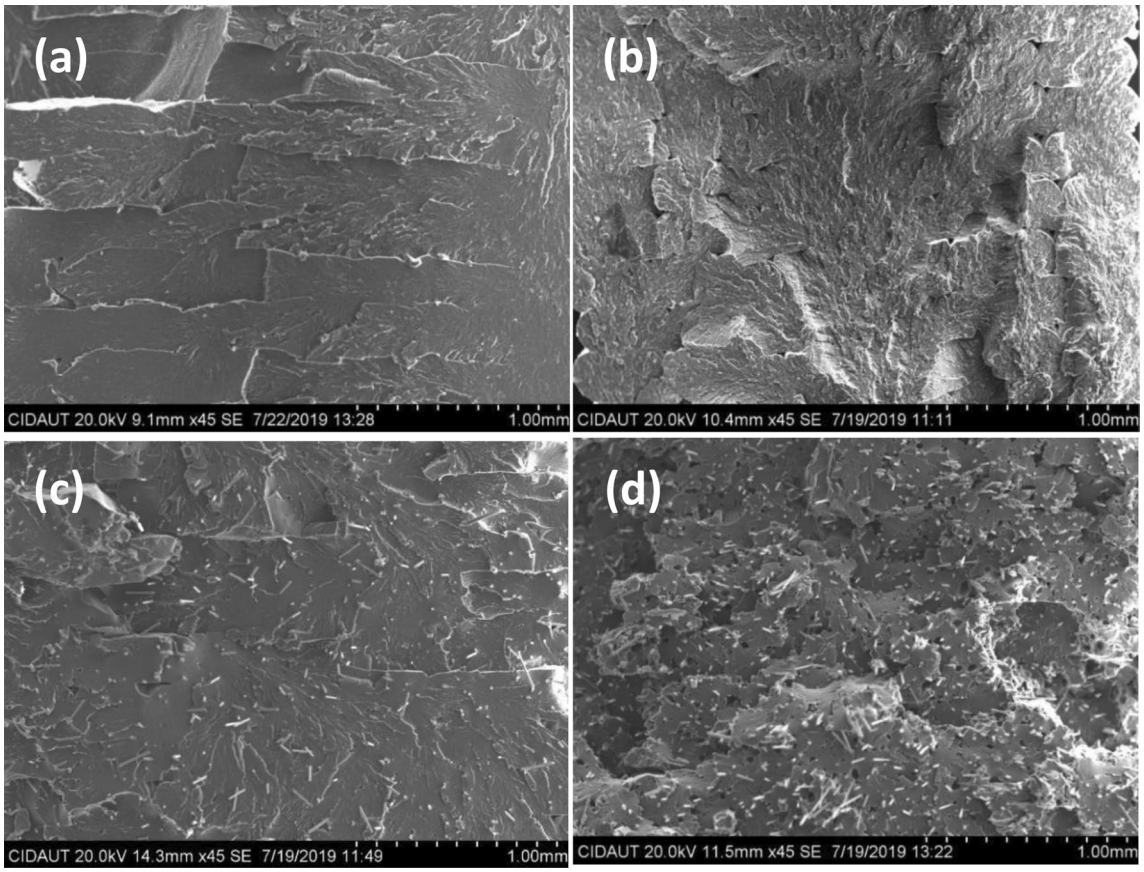

Fig. 12 SEM image of printed samples in *XZ* direction: **a** neat PA11, **b** 15 wt.% of sepiolite-reinforced nanocomposite, **c** 5 wt.% and d) 15 wt.% of glass fibre-reinforced composites

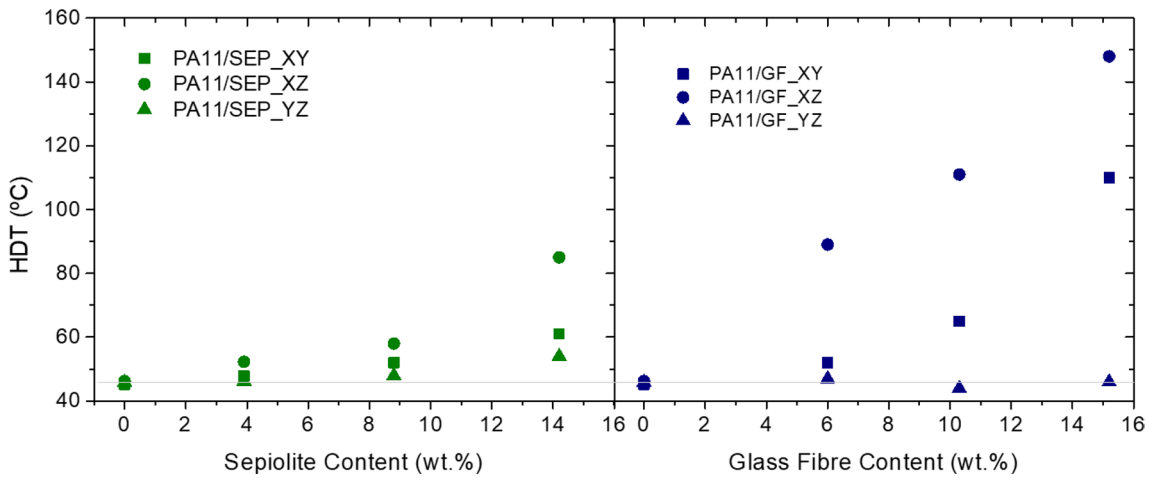

Fig. 13 HDT values of the **a** SEP nanocomposites and, **b** GF composites as a function of the reinforcement content

fibre led to more than three-fold growth. The differences in the obtained results, when comparing different kinds of fibres, are produced by the upper length of the glass fibre. On one hand, it is well known that longer fibres improve creep resistance [55]. On the other hand, longer fibres drive alignment during printing, especially at higher fibre content, resulting in better stress transfer during testing and superior values of HDT.

In terms of HDT, it can be concluded that regardless of the printing direction, glass fibre composites will perform better on parts printed by FFF. However, in parts with equal HDT value (i.e., around 80 °C), composites with 14.2 wt.% of sepiolite can be competitive with its analogue (6 wt.%. GF) in terms of weight and cost reduction. Finally, it has been shown that the length of the glass fibre is affected by processing, so it is not possible to exploit the full benefits of the initial length of the GF in these printed parts in terms of HDT.

4 Conclusions

This work evaluated the mechanical performance of printed parts with bio-based polymers by FFF using different fibrillar reinforcements. The impact of fibre size and nature on the mechanical properties of PA11-based composites by FFF were systematically examined as a function of print orientation and fibre quantity, as well as their relationship with the final microstructural morphology.

The mechanisms of stiffening and energy dissipation on impact, as well as the final morphology of the defects, are different between the two types of composites. Neither SEP nor GF act as nucleating agents in the crystalline system. The fibre-type dependent stiffening is explained by the immobilisation of the chains and in the particular case of SEP by the polymorphism it induces. This explains why SEP is a powerful stiffener at low concentrations in printed parts. Furthermore, the nanofibre has shown greater uniformity in the microstructural porosity, it generates in FFF-printed parts (more isotropic and smaller in size, concentrated only in inter-raster-type defects). This allows the nanocomposites to maintain higher elongation at break and impact energy absorption rates with lower amounts of fibre.

However, the advantages of high fibre length (GF) in activating more efficient energy dissipation mechanisms that improve impact behaviour at high load concentrations are not negligible, as well as the dimensional stability offered to the pieces when working at high temperatures. Therefore, depending on the application, one or the other type of load can be used. Always considering the loss of GF length during processing. It is also important to note that none of the composites studied required special adjustments to the printing parameters. The thermal, rheological, and mechanical characteristics of the materials studied are suitable for this manufacturing technique.

Finally, the best trade-off between the competitive effects of filler reinforcement efficiency and void formation is offered by SEP, in addition to weight savings, cost reduction and carbon footprint reduction. However, unless polymer nanocomposites can be produced on an industrial scale, the use of alternative fillers such as carbon fibres or glass fibres, will remain the industry standard, even if they are not bio-based and do not offer as significant a mechanical improvement as demonstrated.

Supplementary Information The online version contains supplementary material available at https://doi.org/10.1007/s40964-023-00486-9.

Author contributions KCNC conceptualization, methodology, validation, writing—review and editing, formal analysis, and project administration. MH term, conceptualization, methodology, validation, data curation, writing—review and editing and visualization. LEAP data curation; writing—review and editing. FLA formal analysis, software and validation. LOS formal analysis, software and validation. JCM visualization, resources, and project administration. MARP visualization, resources, and funding acquisition and JMPB visualization, resources, project administration and funding acquisition.

Funding This research was funded by UVA Postdoctoral Contract CONVOCATORIA 2020 (KCNC). The authors would also like to thank the Recovery and Resilience Mechanism Funds—Next Generation EU Funds—and the Community of Castilla y León Funds. Complementary Research and Development Plans with the Autonomous Communities in R&D&I actions, of the Component 17. Investment 1.

Declarations

Conflict of interest The authors declare no conflicts of interest.

References

1. Ligon SC, Liska R, Stampfl J et al (2017) Polymers for 3D printing and customized additive manufacturing. Chem Rev 117:10212–10290. https://doi.org/10.1021/acs.chemrev.7b00074
2. Choudhuri A, Wicker R (2015) Energy engineering with frontier additive manufacturing. Aerosp Am 53:59–59
3. Gao W, Zhang Y, Ramanujan D et al (2015) The status, challenges, and future of additive manufacturing in engineering. Comput Aided Des 69:65–89. https://doi.org/10.1016/j.cad.2015.04.001
4. Dilberoglu UM, Gharehpapagh B, Yaman U, Dolen M (2017) The role of additive manufacturing in the era of industry 4.0. Procedia Manuf 11:545–554. https://doi.org/10.1016/j.promfg.2017.07.148
5. Turner BN, Strong R, Gold SA (2014) A review of melt extrusion additive manufacturing processes: I. Process design and modeling. Rapid Prototyp J 20:192–204. https://doi.org/10.1108/RPJ-01-2013-0012
6. Singh S, Singh G, Prakash C, Ramakrishna S (2020) Current status and future directions of fused filament fabrication. J Manuf Process 55:288–306. https://doi.org/10.1016/j.jmapro.2020.04.049
7. Ahmadifar M, Benfriha K, Shirinbayan M, Tcharkhtchi A (2021) Additive manufacturing of polymer-based composites using fused filament fabrication (FFF): a review. Springer Netherlands
8. Gao X, Qi S, Kuang X et al (2021) Fused filament fabrication of polymer materials: a review of interlayer bond. Addit Manuf. https://doi.org/10.1016/j.addma.2020.101658
9. Dey A, Eagle INR, Yodo N (2021) A review on filament materials for fused filament fabrication. J Manuf Mater Process. https://doi.org/10.3390/jmmp5030069
10. Anitha R, Arunachalam S, Radhakrishnan P (2001) Critical parameters influencing the quality of prototypes in fused deposition modelling. J Mater Process Technol 118:385–388. https://doi.org/10.1016/S0924-0136(01)00980-3

11. Tarabanis KA (2001) Path planning in the proteus rapid prototyping system. Rapid Prototyp J 7:241–252. https://doi.org/10.1108/13552540110410440
12. Wohlers Associates (2015) Wohlers report 2015: 3D printing and additive manufacturing state of the industry. Annual Worldwide Progress Report
13. Peterson AM (2019) Review of acrylonitrile butadiene styrene in fused filament fabrication: a plastics engineering-focused perspective. Addit Manuf 27:363–371. https://doi.org/10.1016/j.addma.2019.03.030
14. Sood AK, Ohdar RK, Mahapatra SS (2010) Parametric appraisal of mechanical property of fused deposition modelling processed parts. Mater Des 31:287–295. https://doi.org/10.1016/j.matdes.2009.06.016
15. Ge Q, Qi HJ, Dunn ML (2013) Active materials by four-dimension printing. Appl Phys Lett 103:131901. https://doi.org/10.1063/1.4819837
16. Peng F, Zhao Z, Xia X et al (2018) Enhanced impact resistance of three-dimensional-printed parts with structured filaments. ACS Appl Mater Interfaces 10:16087–16094. https://doi.org/10.1021/acsami.8b00866
17. Wu W, Geng P, Li G et al (2015) Influence of layer thickness and raster angle on the mechanical properties of 3D-printed PEEK and a comparative mechanical study between PEEK and ABS. Materials 8:5834–5846. https://doi.org/10.3390/ma8095271
18. Wu J, Xu X, Zhao Z et al (2018) Study in performance and morphology of polyamide 12 produced by selective laser sintering technology. Rapid Prototyp J 24:813–820. https://doi.org/10.1108/RPJ-01-2017-0010
19. Cai C, Tey WS, Chen J et al (2021) Comparative study on 3D printing of polyamide 12 by selective laser sintering and multi jet fusion. J Mater Process Technol 288:116882. https://doi.org/10.1016/j.jmatprotec.2020.116882
20. Shakeri Z, Benfriha K, Shirinbayan M et al (2021) Mathematical modeling and optimization of fused filament fabrication (Fff) process parameters for shape deviation control of polyamide 6 using taguchi method. Polymers (Basel). https://doi.org/10.3390/polym13213697
21. Herrero M, Peng F, Núñez Carrero KC et al (2018) Renewable Nanocomposites for Additive Manufacturing Using Fused Filament Fabrication. ACS Sustain Chem Eng 6:12393–12402. https://doi.org/10.1021/acssuschemeng.8b02919
22. Herrero M, Asensio M, Núñez K et al (2019) Morphological, thermal, and mechanical behavior of polyamide11/sepiolite bio-nanocomposites prepared by melt compounding and in situ polymerization. Polym Compos 40:E704–E713. https://doi.org/10.1002/pc.24962
23. Jia Y, He H, Peng X et al (2017) Preparation of a new filament based on polyamide-6 for three-dimensional printing. Polym Eng Sci 57:1322–1328. https://doi.org/10.1002/pen.24515
24. Mutlu H, Meier MAR (2010) Castor oil as a renewable resource for the chemical industry. Eur J Lipid Sci Technol 112:10–30. https://doi.org/10.1002/ejlt.200900138
25. Brenken B, Barocio E, Favaloro A et al (2018) Fused filament fabrication of fiber-reinforced polymers: a review. Addit Manuf 21:1–16. https://doi.org/10.1016/j.addma.2018.01.002
26. Tran TQ, Ng FL, Kai JTY et al (2022) Tensile strength enhancement of fused filament fabrication printed parts: a review of process improvement approaches and respective impact. Addit Manuf 54:102724. https://doi.org/10.1016/j.addma.2022.102724
27. Iqbal Khan Z, Habib U, Binti Mohamad Z et al (2022) Mechanical and thermal properties of sepiolite strengthened thermoplastic polymer nanocomposites: a comprehensive review. Alex Eng J 61:975–990. https://doi.org/10.1016/j.aej.2021.06.015
28. Wang Z, Xiao H (2009) Nanocomposites: recent development and potential automotive applications. SAE Int J Mater Manuf 1:631–640. https://doi.org/10.4271/2008-01-1263
29. Herrero M, Núñez K, Gallego R et al (2018) Sepiolite as replacement of short glass fibre in polyamide composites for injection moulding applications. Appl Clay Sci 162:129–137. https://doi.org/10.1016/j.clay.2018.06.006
30. Tekinalp HL, Kunc V, Velez-Garcia GM et al (2014) Highly oriented carbon fiber–polymer composites via additive manufacturing. Compos Sci Technol 105:144–150. https://doi.org/10.1016/j.compscitech.2014.10.009
31. Zhang Q, Mo Z, Liu S, Zhang H (2000) Influence of annealing on structure of Nylon 11. Macromolecules 33:5999–6005. https://doi.org/10.1021/ma000298d
32. Pérez-Tamarit S, Solórzano E, Hilger A et al (2018) Multi-scale tomographic analysis of polymeric foams: a detailed study of the cellular structure. Eur Polym J 109:169–178. https://doi.org/10.1016/j.eurpolymj.2018.09.047
33. Logakis E, Pandis C, Peoglos V, Pissis P, Stergiou C, Pionteck J, Potschke P, Matej Micusik MO (2009) Structure-property relationships in polyamide 6/multi-walled carbon nanotubes nanocomposites. J Polym Sci B Polym Phys 47:764–774. https://doi.org/10.1002/polb
34. Liu T, Chen D, Phang IY, Wei C (2014) Studies on crystal transition of polyamide 11 nanocomposites by variable-temperature X-ray diffraction. Chin J Polym Sci 32:115–122. https://doi.org/10.1007/s10118-014-1383-3
35. Mago G, Kalyon DM, Fisher FT (2011) Nanocomposites of polyamide-11 and carbon nanostructures: development of microstructure and ultimate properties following solution processing. J Polym Sci B Polym Phys 49:1311–1321. https://doi.org/10.1002/polb.22311
36. Lincoln DM, Vaia RA, Wang Z-G, Hsiao BS (2001) Secondary structure and elevated temperature crystallite morphology of nylon-6/layered silicate nanocomposites. Polymer (Guildf) 42:1621–1631. https://doi.org/10.1016/S0032-3861(00)00414-6
37. Murthy NS (1991) Metastable crystalline phases in nylon 6. Polym Commun 32:301–305
38. Zhang G, Li Y, Yan D (2004) Polymorphism in nylon-11/montmorillonite nanocomposite. J Polym Sci B Polym Phys 42:253–259. https://doi.org/10.1002/polb.10680
39. Liu T, Ping Lim K, Chauhari Tjiu W et al (2003) Preparation and characterization of nylon 11/organoclay nanocomposites. Polymer (Guildf) 44:3529–3535. https://doi.org/10.1016/S0032-3861(03)00252-0
40. Zhang X, Yang G, Lin J (2006) Crystallization behavior of nylon 11/montmorillonite nanocomposites under annealing. J Appl Polym Sci 102:5483–5489. https://doi.org/10.1002/app.23900
41. Oliver-Ortega H, Méndez J, Mutjé P et al (2017) Evaluation of thermal and thermomechanical behaviour of bio-based polyamide 11 based composites reinforced with lignocellulosic fibres. Polymers (Basel) 9:522. https://doi.org/10.3390/polym9100522
42. Nair SS, Ramesh C, Tashiro K (2006) Crystalline phases in Nylon11 studies using HTWAXS and HTFTIR. Macromolecules 39:2841–2848. https://doi.org/10.1021/ma052597e
43. Dickson A, Abourayana H, Dowling D (2020) 3D printing of fibre-reinforced thermoplastic composites using fused filament fabrication—a review. Polymers (Basel) 12:1–18
44. Xie S, Zhang S, Wang F et al (2007) Preparation, structure and thermomechanical properties of nylon-6 nanocomposites with lamella-type and fiber-type sepiolite. Compos Sci Technol 67:2334–2341. https://doi.org/10.1016/j.compscitech.2007.01.012
45. Abbott AC, Tandon GP, Bradford RL et al (2018) Process-structure-property effects on ABS bond strength in fused filament fabrication. Addit Manuf 19:29–38. https://doi.org/10.1016/j.addma.2017.11.002

46. Walter R, Friedrich K, Gurka M (2018) Characterization of mechanical properties of additively manufactured polymers and composites. p 020033
47. Nguyen NA, Bowland CC, Naskar AK (2018) A general method to improve 3D-printability and inter-layer adhesion in lignin-based composites. Appl Mater Today 12:138–152. https://doi.org/10.1016/j.apmt.2018.03.009
48. Rostom S, Dadmun MD (2019) Improving heat transfer in fused deposition modeling with graphene enhances inter filament bonding. Polym Chem 10:5967–5978. https://doi.org/10.1039/C9PY00832B
49. Weng Z, Wang J, Senthil T, Wu L (2016) Mechanical and thermal properties of ABS/montmorillonite nanocomposites for fused deposition modeling 3D printing. Mater Des 102:276–283. https://doi.org/10.1016/j.matdes.2016.04.045
50. Travieso-Rodriguez JA, Zandi MD, Jerez-Mesa R, Lluma-Fuentes J (2020) Fatigue behavior of PLA-wood composite manufactured by fused filament fabrication. J Market Res 9:8507–8516. https://doi.org/10.1016/j.jmrt.2020.06.003
51. Thaler D, Aliheidari N, Ameli A (2019) Mechanical, electrical, and piezoresistivity behaviors of additively manufactured acrylonitrile butadiene styrene carbon nanotube nanocomposites. Smart Mater Struct 28:084004. https://doi.org/10.1088/1361-665X/ab256e
52. Khan AN, Ahmed BA (2015) Comparative study of Polyamide 6 reinforced with glass fibre and montmorillonite. Polym Bull 72:1207–1216. https://doi.org/10.1007/s00289-015-1333-4
53. Cotterell B, Chia JYH, Hbaieb K (2007) Fracture mechanisms and fracture toughness in semicrystalline polymer nanocomposites. Eng Fract Mech 74:1054–1078. https://doi.org/10.1016/j.engfracmech.2006.12.023
54. Phang IY, Liu T, Mohamed A et al (2005) Morphology, thermal and mechanical properties of nylon 12/organoclay nanocomposites prepared by melt compounding. Polym Int 54:456–464. https://doi.org/10.1002/pi.1721
55. Thomason JL (2007) Structure–property relationships in glass reinforced polyamide, part 2: the effects of average fiber diameter and diameter distribution. Polym Compos 28:331–343. https://doi.org/10.1002/pc.20260
56. Abd Rahman N, Hassan A, Heidarian J (2018) Effect of compatibiliser on the properties of polypropylene/glass fibre/nanoclay composites. Polimeros 28:103–111. https://doi.org/10.1590/0104-1428.2357
57. Hassan A, Salleh NM, Yahya R, Sheikh MRK (2011) Fiber length, thermal, mechanical, and dynamic mechanical properties of injection-molded glass-fiber/polyamide 6,6: plasticization effect. J Reinf Plast Compos 30:488–498. https://doi.org/10.1177/0731684410397898
58. Harris M, Potgieter J, Archer R, Arif KM (2019) Effect of material and process specific factors on the strength of printed parts in fused filament fabrication: a review of recent developments. Materials. https://doi.org/10.3390/ma12101664